

1  
2  
3  
4 **Hypoxia inducible factors regulate infectious SARS-CoV-2, epithelial damage and**  
5 **respiratory symptoms in a hamster COVID-19 model.**  
6  
7

8 Peter A.C. Wing<sup>1,2&</sup>, Maria Prange-Barczynska<sup>2,3</sup>, Amy Cross<sup>4</sup>, Stefania Crotta<sup>5</sup>, Claudia Orbegozo  
9 Rubio<sup>2</sup>, Xiaotong Cheng<sup>2,3</sup>, James M. Harris<sup>2</sup>, Xiaodong Zhuang<sup>2</sup>, Rachel L. Johnson<sup>6</sup>, Kathryn A.  
10 Ryan<sup>6</sup>, Yper Hall<sup>6</sup>, Miles W. Carroll<sup>2</sup>, Fadi Issa<sup>4</sup>, Peter Balfe<sup>2</sup>, Andreas Wack<sup>5</sup>,  
11 Tammie Bishop<sup>2,3</sup>, Francisco J. Salguero<sup>6\*</sup> and Jane A. McKeating<sup>1,2\*&</sup>

12  
13 \*Shared Senior Authorship, <sup>&</sup>Corresponding authors

14 Corresponding authors: Jane A McKeating and Peter AC Wing Tel: +44(0)1865 612894.

15 jane.mckeating@ndm.ox.ac.uk; ORCID: 0000-0002-7229-5886.

16 peter.wing@ndm.ox.ac.uk; ORCID: 0000-0002-2354-3281.

17  
18  
19 1. Chinese Academy of Medical Sciences Oxford Institute, University of Oxford, Oxford UK.  
20 2. Nuffield Department of Medicine, University of Oxford, Oxford UK.  
21 3. Ludwig Institute for Cancer Research, University of Oxford, Oxford UK.  
22 4. Radcliffe Department of Surgery, University of Oxford, UK.  
23 5. Immunoregulation Laboratory, The Francis Crick Institute, London UK.  
24 6. United Kingdom Health Security Agency (UKHSA), Porton Down, Salisbury, UK.  
25  
26

27 **ABSTRACT**

28 Understanding the host pathways that define susceptibility to SARS-CoV-2 infection and disease are  
29 essential for the design of new therapies. Oxygen levels in the microenvironment define the  
30 transcriptional landscape, however the influence of hypoxia on virus replication and disease in animal  
31 models is not well understood. In this study, we identify a role for the hypoxic inducible factor (HIF)  
32 signalling axis to inhibit SARS-CoV-2 infection, epithelial damage and respiratory symptoms in Syrian  
33 hamsters. Pharmacological activation of HIF with the prolyl-hydroxylase inhibitor FG-4592 significantly  
34 reduced the levels of infectious virus in the upper and lower respiratory tract. Nasal and lung epithelia  
35 showed a reduction in SARS-CoV-2 RNA and nucleocapsid expression in treated animals.  
36 Transcriptomic and pathological analysis showed reduced epithelial damage and increased  
37 expression of ciliated cells. Our study provides new insights on the intrinsic antiviral properties of the  
38 HIF signalling pathway in SARS-CoV-2 replication that may be applicable to other respiratory  
39 pathogens and identifies new therapeutic opportunities.

41 **INTRODUCTION**

42 COVID-19, caused by the coronavirus SARS-CoV-2, is a global health issue with more than 5.5  
43 million fatalities to date. Vaccination has reduced both the number of hospitalisations and mortality  
44 due to COVID-19 (Singanayagam et al., 2021; Voysey et al., 2021). However, the emergence of  
45 variants, such as Omicron, that show reduced sensitivity to vaccine-induced immunity (Dejnirattisai et  
46 al., 2021a; Dejnirattisai et al., 2021b; Liu et al., 2021), provide the potential for new waves of infection.  
47 The primary site of SARS-CoV-2 infection is the upper respiratory epithelia with diminishing levels of  
48 infection in distal areas of the lung (Hou et al., 2020). A defining feature of severe COVID-19  
49 pneumonitis is systemic low oxygen (hypoxaemia), which can lead to organ failure and death through  
50 acute respiratory distress syndrome (Huang et al., 2020; Li et al., 2020). At the cellular level, hypoxia  
51 induces substantial changes to the host transcriptional landscape regulating a diverse array of  
52 biological pathways that are orchestrated by hypoxic inducible factors (HIFs). When oxygen is  
53 abundant, newly synthesised HIF $\alpha$  subunits are hydroxylated by HIF prolyl-hydroxylase domain  
54 (PHD) enzymes resulting in their proteasomal degradation. Under hypoxic conditions the PHD  
55 enzymes are inactive and stabilised HIF $\alpha$  dimerizes with HIF-1 $\beta$ , translocates to the nucleus, and  
56 promotes the transcription of genes involved in erythropoiesis, glycolysis, pulmonary vasomotor  
57 control, and immune regulation (Kaelin and Ratcliffe, 2008; Palazon et al., 2014; Urrutia and  
58 Aragones, 2018). HIF-target genes can vary between cell types allowing a flexible response to  
59 diverse physiological signals (Schodel et al., 2011).

60

61 Under normal physiological conditions, the lungs provide an oxygen rich environment, however, an  
62 increasing body of literature shows a role for hypoxia in the inflamed airway epithelium (Page et al.,  
63 2021). Transcriptomic analysis of post-mortem COVID-19 pulmonary tissue shows an association  
64 between hypoxic signalling and inflammatory responses (Cross et al., 2021; Sposito et al., 2021).  
65 While HIFs may drive inflammation in certain settings, HIF-1 $\alpha$  has been shown to suppress the  
66 inflammatory response in bronchial epithelial cells reducing expression of IL-6 and IP10 (Polke et al.,  
67 2017). This dual role of HIFs highlights the importance of the cellular environment in which hypoxia  
68 occurs.

69

70 HIFs modulate the replication of a wide number of viruses (Liu et al., 2020), enhancing the replication  
71 of hepatitis B (Wing et al., 2021b) and Epstein Barr viruses (Jiang et al., 2006; Kraus et al., 2017) via  
72 direct binding to their viral DNA genomes. In contrast, HIFs inhibit influenza A virus replication in lung  
73 epithelial models of infection (Zhao et al., 2020). These differing outcomes may reflect variable  
74 oxygen levels at the site of virus replication in the body. Several respiratory pathogens including  
75 Influenza (Ren et al., 2019), Rhinovirus (Gualdoni et al., 2018) and Respiratory Syncytial virus  
76 (Haeberle et al., 2008) induce anaerobic glycolysis via activation of the HIF-1 $\alpha$  signalling axis,  
77 suggesting a role for viruses to manipulate this pathway. A greater understanding of the oxygen  
78 microenvironment in the healthy and inflamed lung will inform our understanding of mucosal host-  
79 pathogen interactions.

80

81 We have reported that hypoxic activation of HIF-1 $\alpha$  inhibits SARS-CoV-2 entry and replication in  
82 primary and immortalised lung epithelial cells (Wing et al., 2021a). HIF-1 $\alpha$  downregulates the  
83 expression of two key entry factors ACE2 and TMPRSS2, thereby limiting SARS-CoV-2  
84 internalisation, whilst also restricting the establishment of viral replication complexes. These data  
85 show an essential role for hypoxia/HIF-1 $\alpha$  in multiple aspects of the SARS-CoV-2 life cycle and it is  
86 timely to address the role of HIFs in an immune competent animal model of COVID-19 disease.

87

88 HIFs can be activated by drugs that inhibit the PHDs which are currently used for the treatment of  
89 renal anaemia (Akizawa et al., 2020a; Akizawa et al., 2020b; Akizawa et al., 2020c; Akizawa et al.,  
90 2020d; Chen et al., 2019a; Chen et al., 2019b). We evaluated the ability of the PHD inhibitor FG-4592  
91 (Roxadustat) to inhibit SARS-CoV-2 replication and pathogenesis in Golden Syrian hamsters, that  
92 shows similar features to human disease including lung pathology and damage to the ciliated epithelia  
93 (Chan et al., 2020; de Melo et al., 2021; Imai et al., 2020; Rosenke et al., 2020; Sia et al., 2020).  
94 Treatment of infected hamsters with FG-4592, either prophylactically or after infection, reduced the  
95 infectious viral burden and respiratory symptoms. Our study provides new information on how the HIF  
96 signalling pathway influences SARS-CoV-2 replication that may be applicable to other respiratory  
97 pathogens and suggests new preventative and therapeutic opportunities

98

## 99 RESULTS

### 100 **Orally administered FG-4592 activates HIFs in the lung and limits SARS-CoV-2 disease 101 severity.**

102 To assess the effect of FG-4592 on SARS-CoV-2 infection, hamsters were treated with 30mg/kg of  
103 drug twice daily by oral gavage commencing either 24h pre- or 24h post-viral challenge. This regimen  
104 was based on previous FG-4592 dosing protocols in mice (Schley et al., 2019; Wing et al., 2021a)  
105 and clinical studies (Provenzano et al., 2016). In the control group, animals were treated with vehicle  
106 24h prior to infection which continued throughout the study in the same manner as treated animals  
107 (**Fig.1A**). Hamsters were infected with SARS-CoV-2 (Australia/VIC01/2020 or VIC01) by intranasal  
108 delivery of  $5 \times 10^4$  plaque forming units (PFU), which is sufficient to cause clinical signs and respiratory  
109 lesions (Huo et al., 2021; Rosenke et al., 2020; Ryan et al., 2021). Weight and body temperature  
110 were recorded and clinical signs such as laboured breathing, ruffled fur and lethargy measured twice  
111 daily to provide a clinical score (described in **Supplementary Table 1**). Infectious virus in the upper  
112 respiratory tract was measured in nasal washes and throat swabs collected at 1-, 2- and 4-days post-  
113 infection. The study was terminated at 4 days post-infection based on studies reporting the detection  
114 of infectious virus in the upper respiratory tract (**Fig.1A**) (Chan et al., 2020; Imai et al., 2020; Rosenke  
115 et al., 2020).

116

117 We observed a significant reduction in body temperature and a loss of body weight in all treatment  
118 groups (**Fig.1B**), in line with the clinical presentation of SARS-CoV-2 in this model (Chan et al., 2020;  
119 Nouailles et al., 2021; Rosenke et al., 2020). No significant differences in animal weight or  
120 temperature were noted between the treatment groups, suggesting that FG-4592 was well-tolerated

121 (Fig.1B). The first signs of disease were observed at day 2 post-infection, further increasing by day 4  
122 in the control group primarily due to the onset of laboured breathing (Fig.1C, **Supplementary Table**  
123 **1**). Animals treated with FG-4592 showed a significant improvement in their clinical score, particularly  
124 in the post-infection treatment group (Fig.1C). Further, while all animals in the control vehicle group  
125 presented with laboured breathing, this was only observed in 2/6 animals in the pre-infection  
126 treatment group and none of the hamsters in the post-infection treatment group.

127

128 As HIF expression following systemic PHI treatment is transient and difficult to detect (Chan et al.,  
129 2016), we evaluated FG-4592 efficacy by assessing HIF activation of erythropoietin stimulated  
130 erythropoiesis by measuring immature red blood cells (reticulocytes). Blood smears from terminal  
131 blood samples showed increased reticulocyte counts compared to vehicle, consistent with effective  
132 drug treatment (Fig.1D). To evaluate whether FG-4592 activated HIFs in the lung we assessed  
133 pulmonary expression of the HIF target gene Endothelin-1 (*Edn-1*) (Hickey et al., 2010) and noted a  
134 modest but significant induction of mRNA (Fig.1E). Furthermore, we noted a decrease in mRNA  
135 levels of the viral entry receptor *Ace2* in the lungs of treated hamsters (Fig.1F), supporting our  
136 previous findings (Wing et al., 2021a). To understand the PHI-driven changes in pulmonary gene  
137 expression we sequenced RNA from the lung tissue of vehicle, FG-4592 pre- or post- infection groups  
138 and observed an induction of 47 and 63 genes respectively, including HIF target genes such as *Edn-1*  
139 and *Bnip3* (**Supplementary Fig.1A**). To assess whether all animals responded to FG-4592 we  
140 evaluated transcript levels of the common HIF-upregulated genes. Hierarchical cluster analysis  
141 separated the vehicle and treated animals and showed comparable activation in the pre- and post-  
142 infection treatment groups, demonstrating that animals had responded in a similar manner  
143 (**Supplementary Fig.1B**). Together these data show that FG-4592 is well tolerated, activates HIF-  
144 transcriptional responses in the lung and reduces symptoms of SARS-CoV-2 infection.

145

#### 146 **FG-4592 reduces infectious SARS-CoV-2 in upper and lower respiratory tract.**

147 The course of SARS-CoV-2 disease in the Syrian hamster is transient, with the onset of clinical  
148 symptoms peaking between 4-6 days post-infection followed by the development of neutralising  
149 antibodies and viral clearance within 8-15 days (Chan et al., 2020; Sia et al., 2020). To assess the  
150 effect of HIFs on SARS-CoV-2 replication we measured viral RNA by qPCR and infectious virus by  
151 plaque assay using Vero-TMPRSS2 cells (**Supplementary Fig.2**). High levels of viral RNA and  
152 infectious SARS-CoV-2 were detected in the nasal washes and throat swabs sampled at day 1 post-  
153 infection in the vehicle group, which declined over the course of the study (Fig.2A-B). Pre-treatment  
154 with FG-4592 resulted in a 1-log reduction in the infectious viral burden in both nasal washes and  
155 throat swabs at day 2 post-infection (Fig.2A-B). Similarly, animals treated post-infection showed  
156 significantly reduced levels of infectious virus by day 4. In contrast, drug treatment had a negligible  
157 effect on the total viral RNA levels measured in either the nasal washes or throat swabs (Fig.2A-B).  
158 We also measured the burden of infectious virus in the lungs at the end of the study and showed a  
159 significant reduction in the treated animals (Fig.2C). However, there was no substantial change in  
160 total or genomic viral RNA (gRNA) (Fig.2C, **Supplementary Fig.3**). Together these data demonstrate

161 that PHI treatment before or after infection significantly reduced the infectious viral burden in the  
162 upper and lower respiratory tract of infected hamsters.

163

164

165 **FG-4592 reduces SARS-CoV-2 sub-genomic RNAs in the lung.**

166 Since FG-4592 reduced the level of infectious virus in the lung we were interested to assess whether  
167 treatment impacts the viral transcriptome. Mapping the viral reads across the 30kb SARS-CoV-2  
168 genome demonstrated an increasing read depth from ORF1ab to the 3'UTR consistent with the  
169 transcription of sub-genomic (sg) RNAs (**Supplementary Fig.4A**). In addition to the gRNA, the viral  
170 transcriptome includes 9 canonical sub-genomic (sg) RNAs that encode the structural proteins, which  
171 are essential for the genesis of nascent virus particles. Quantifying the junction spanning reads  
172 between the common 5' leader sequence and the start of each sgRNA (as previously described (Kim  
173 et al., 2020)), enabled us to infer their approximate abundance. FG-4592 reduced the abundance of  
174 most sgRNAs with a greater variability in the treated groups and a significant reduction in the  
175 nucleocapsid (N) transcript, the most abundant of the viral RNAs (**Fig.3A**). We extended these  
176 observations to study the effect of HIF-signalling in SARS-CoV-2 transcription in the lung Calu-3  
177 epithelial cell line (Sampaio et al., 2021) and showed a significant reduction in S, E, M, ORF6,  
178 ORF7A, ORF7B, ORF8 and N junction spanning reads (**Fig.3B**). The relative abundance of SARS-  
179 CoV-2 transcripts were similar in Calu-3 and infected hamster lung tissue. Analysing samples from  
180 the infected Calu-3 cells by northern blotting confirmed that FG-4592 treatment reduced viral  
181 transcripts (**Fig.3C**). Furthermore, FG-4592 treatment inhibited N protein expression in infected Calu-  
182 3 cells (**Fig.3D**), providing an explanation for the antiviral activity of HIFs.

183

184 Finally, we assessed SARS-CoV-2 sequence variation to determine whether treatment associated  
185 with genetic changes. Viral sequences were conserved across the genome in the vehicle or treated  
186 lung tissues (**Supplementary Fig.4B**) and no changes in the consensus sequence were seen in the  
187 treated animals or Calu-3 cells, with 100% conservation of the nucleotide sequence across the  
188 genome (**Supplementary Table 2**). Together these data show that FG-4592 treatment had no effect  
189 on the sequence of SARS-CoV-2 in the lung but reduced sgRNAs.

190

191 **Spatial analysis of SARS-CoV-2 RNA and nucleocapsid expression in the respiratory tract.**

192 As FG-4592 reduced the clinical signs and levels of infectious virus in the upper and lower respiratory  
193 tract we explored the impact of treatment on virus-associated pathology. Sequential sections from the  
194 nasal cavity and lung tissue were stained with haematoxylin and eosin (H&E) and with RNA-scope *in*  
195 *situ* hybridization (ISH) probes targeting the Spike gene to assess the tissue distribution of SARS-  
196 CoV-2 RNA. We noted extensive inflammatory cell exudate in the nasal cavity and mild to moderate  
197 necrosis in both the olfactory and respiratory epithelia (**Supplementary Fig.5A-C**). We assessed  
198 these pathological changes using a semi-quantitative scoring system and showed a reduction in the  
199 nasal histopathological score in the post-infection treatment group (**Fig.4B, Supplementary Table 3**).  
200 Viral RNA primarily localised to the epithelia and exudate in the nasal cavity and FG-4592 reduced

201 epithelial staining, the major site of virus replication (**Fig.4B**). A similar observation was noted for viral  
202 RNA signals in the exudate (**Fig.4B**); however, these results may be compromised by the daily  
203 collection of nasal washes.

204

205 In agreement with previous studies (Dowall et al., 2021; Gruber et al., 2020; Nouailles et al., 2021),  
206 SARS-CoV-2 infected lung tissue showed pulmonary lesions consisting of broncho-interstitial  
207 pneumonia extending into the alveoli and multifocal areas of consolidation, consistent with  
208 inflammatory cell infiltration and oedema (**Fig.4A, Supplementary Fig.5**). Digital image analysis  
209 showed that FG-4592 treatment did not alter the severity of lung histopathology (**Fig.4C**). Viral RNA  
210 was detected in the bronchiolar epithelia, bronchiolar inflammatory exudates, as well as in the lung  
211 parenchyma of the control vehicle animals (**Fig.4A**) and FG-4592 treatment had no detectable effect  
212 on the viral RNA signals in the parenchyma or airways (**Fig.4C**).

213

214 To extend these observations we stained the infected nasal and lung sections for SARS-CoV-2 N  
215 antigen expression by immunohistochemistry (IHC). Within the nasal cavity, N primarily localised to  
216 the epithelia and exudate (**Fig.5A**), consistent with the detection of S-gene transcripts. Semi-  
217 quantitative scoring of the nasal cavity sections showed reduced N antigen expression in the treated  
218 animals, most notably in the epithelia of post-infection treated samples (**Fig.5B**). Within the lung, N  
219 staining localised to the airways and lung parenchyma (**Fig.5C**), and we noted a significant reduction  
220 of parenchymal staining in the post-infection treated animals (**Fig.5D**). In summary, histopathological  
221 analysis shows that PHI treatment reduced SARS-CoV-2 RNA and N antigen levels in the nasal  
222 epithelia and exudate, consistent with the reduction in infectious viral burden.

223

#### 224 **FG-4592 reduces ciliated epithelial damage in the lung.**

225 To understand the global host response, we sequenced lung tissue from SARS-CoV-2 infected  
226 (vehicle control) and uninfected hamsters. Infection induced substantial changes in the lung  
227 transcriptome compared to uninfected tissue; with an up-regulation of pathways involved in  
228 inflammation and down-regulation of genes involved in cilium organisation and assembly (**Fig.6A-B**).  
229 Analysing inflammatory gene expression using genes from the molecular signature database  
230 (Liberzon et al., 2015) showed that FG-4592 had a modest effect on the lung inflammasome  
231 (**Supplementary Fig.6**). Of note, expression of the viral entry receptors *Ace2* and *Tmprss2* were  
232 significantly downregulated ( $\log_2$  fold change of -1.45 and -1.52 respectively) in the infected tissue,  
233 likely reflecting viral cytopathology (Cross et al., 2021). Loss of ciliated epithelial cells is a key feature  
234 of COVID-19 resulting from damage to the airway epithelia (Pizzorno et al., 2020; Robinot et al.,  
235 2021; Zhu et al., 2020). To examine whether FG-4592 treatment reduced the level of epithelial  
236 damage we used the reported compendium of cilia-related genes (van Dam et al., 2019) to evaluate  
237 gene expression in the pulmonary transcriptome of vehicle and FG-4592 treated animals. A similar  
238 pattern of cilia-related gene expression was noted in the vehicle and pre-infection treatment group,  
239 with most genes showing a marked down-regulation (**Fig.6C**). However, the virus induced down-  
240 regulation of ciliated gene expression was less apparent in animals treated with FG-4592 post-

241 infection (**Fig.6D**). To gain further insight as to whether FG-4592 treatment affects the level of ciliated  
242 cells we stained nasal and lung sections for  $\alpha$ -tubulin and club cell secretory protein (CCSP), markers  
243 of ciliated cells and secretory cells, respectively. We observed a substantial reduction in  $\alpha$ -tubulin and  
244 CCSP staining in the infected lung (**Fig.6E**) and nasal cavity (**Supplementary Fig.6**), consistent with  
245 virus-induced loss of ciliated cells (**Fig.6E**). While limited staining was observed in the lung sections  
246 from the pre-treated animals, we noted a restoration of  $\alpha$ -tubulin expression in post-infection treated  
247 sections, in line with our transcriptomic analysis. Together these data show that a loss of ciliated cells  
248 in the respiratory tract is a prominent feature of SARS-CoV-2 infection and FG-4592 treatment may  
249 offer some protection from this severe pathological change.

250

## 251 **DISCUSSION**

252 In this study we evaluated the antiviral potential of FG-4592 in the Syrian hamster model of SARS-  
253 CoV-2 infection. Treating animals pre- or post-infection reduced the levels of infectious virus and  
254 improved clinical symptoms. The drug was well tolerated, with no adverse reactions reported in any of  
255 the treated animals. Despite treatment showing a significant reduction in the levels of infectious virus,  
256 bulk PCR quantification of viral RNA in the nasal washes and throat swabs were unchanged. An  
257 earlier study of SARS-CoV-2 infection in Syrian hamsters reported a relatively short contagious period  
258 that associated with the detection of infectious virus (Dowall et al., 2021). However, SARS-CoV-2  
259 RNA can persist in the respiratory tract long after the communicable period has passed (Chan et al.,  
260 2020; Dowall et al., 2021; Sia et al., 2020). SARS-CoV-2 RNA genomes are highly structured, and  
261 this may contribute to their persistence (Huston et al., 2021; Simmonds et al., 2021). Several reviews  
262 have reported a discrepancy between viral RNA levels and the detection of infectious virus in clinical  
263 samples (Cevik et al., 2021; La Scola et al., 2020; Walsh et al., 2020). While quantitative PCR  
264 measurement is the gold standard for SARS-CoV-2 diagnosis, this method only detects the viral  
265 nucleic acid and not the infectious capacity of virus particles. An important factor to consider is the  
266 cellular location of the viral RNA in the respiratory tract, where ISH probing of infected nasal tissue  
267 revealed SARS-CoV-2 RNA in both the nasal exudate and epithelia. We hypothesise the exudate will  
268 comprise extracellular encapsidated viral RNA and processed viral particles in immune cells and does  
269 not reflect sites of active virus replication. Our *in-situ* analysis highlights a significant reduction of viral  
270 RNA in the nasal epithelia of FG-4592 treated animals, demonstrating antiviral drug activity at the  
271 primary site of replication.

272

273 While the disconnect between viral RNA levels and infectivity is not well understood in a clinical  
274 setting, we would predict that drugs inhibiting the level of infectious virus in the upper respiratory tract  
275 will reduce virus transmission. The recently approved anti-viral drug Molnupiravir showed a negligible  
276 effect on viral RNA or infectious titre in respiratory samples when tested in Syrian hamsters (Rosenke  
277 et al., 2021). Yet both Molnupiravir and FG-4592 treatments were associated with significant  
278 reductions in the burden of infectious virus in the lung. While both drugs have contrasting  
279 mechanisms of action, the ability of FG-4592 to limit viral replication highlights the value of targeting  
280 host pathways that are essential for viral replication in concert with the development of direct-acting

281 antiviral (DAA) agents. A promising area for future development is a combined treatment of PHI and  
282 DAAAs such as Molnupiravir or the recently approved protease inhibitor Nirmatrelvir (Owen et al.,  
283 2021). Previous strategies of DAA monotherapies for the treatment of HIV and HCV selected for drug  
284 resistant viruses, reinforcing the value of combination therapies that result in a high barrier to the  
285 development of anti-viral resistance (Hiscox et al., 2021). Our analysis of the SARS-CoV-2 sequences  
286 showed no evidence of mutational change in treated animals. However, the viral transcriptome in the  
287 lung showed differences in the abundance of sgRNAs in the treated animals, similar to our  
288 observations with infected Calu-3 cells where FG-4592 significantly reduced sgRNAs and N protein  
289 expression. These data show a role for HIFs in regulating SARS-CoV-2 sgRNA levels that could be  
290 explained by changes in the genesis or maintenance of viral replication complexes, in line with our  
291 previous observations (Wing et al., 2021a).

292

293 An important finding of this study was the improved clinical score in the treated animals. FG-4592  
294 substantially reduced the incidence of laboured breathing in the infected animals, irrespective of  
295 treatment grouping, that may be attributed to the increased levels of erythropoiesis resulting in  
296 improved blood oxygenation in the infected hamsters. These results justify future studies to evaluate  
297 how improving blood oxygenation impacts the clinical outcome of SARS-CoV-2 infection.

298

299 Histopathological analysis of pulmonary tissue showed that a short duration of FG-4592 treatment  
300 improved virus-induced pathology in the upper respiratory tract. Lungs from the treated animals  
301 showed fewer areas of consolidation and pulmonary lesions, particularly in the post-infection  
302 treatment group. An earlier study reported that SARS-CoV-2 induced lung pathology in this  
303 experimental model peaked at 5 days post-infection, after which tissue injury recovered along with  
304 viral clearance (Rosenke et al., 2020). Since the primary goal of this study was to evaluate the effect  
305 of PHIs on viral replication rather than pathological changes, we predict that longer PHI treatment  
306 times would have more pronounced effects on pulmonary pathology and potentially improve recovery  
307 times.

308

309 A key feature of SARS-CoV-2 infection is the profound loss of the ciliary layer in the respiratory tract  
310 (Pizzorno et al., 2020; Robinot et al., 2021; Zhu et al., 2020); induced either by direct infection of  
311 these cells and their subsequent dedifferentiation (Robinot et al., 2021) or loss by cytopathic infection.  
312 The resulting impairment in mucociliary clearance limits the removal of infiltrating viral, bacterial, or  
313 fungal pathogens that can lead to secondary infections with antibiotic resistant strains of  
314 *Staphylococcus aureus* and *Klebsiella pneumoniae* (Manohar et al., 2020), the incidence of which  
315 markedly increases in critically ill patients (Alanio et al., 2020; Manohar et al., 2020). Our lung  
316 transcriptomic analysis highlighted the altered expression of genes involved in ciliated cell function in  
317 FG-4592 treated animals. Components of the centrosome, important for cilia formation, are regulated  
318 by PHDs and hypoxia increases their expression (Moser et al., 2013), providing a potential  
319 mechanism for our observation. Nonetheless, we are unable to assess whether treatment prevents  
320 infection of ciliated cells or promotes their recovery. Staining tissue sections for  $\alpha$ -tubulin expression,

321 a marker for ciliated cells, in the upper and lower respiratory tract shows the considerable impact of  
322 infection on the abundance of ciliated cells. Importantly, lung sections from animals treated with FG-  
323 4592 post-infection showed elevated levels of ciliated cell staining, that may reflect differences in the  
324 transcriptional response of infected cells to PHIs. Healthy cells will trigger reactions enabling them to  
325 adapt to hypoxia such as switching from oxidative phosphorylation to glycolysis (Semenza, 2011),  
326 however, SARS-CoV-2 infection may alter the cellular response to hypoxia potentially exacerbating  
327 necrosis, cytokine expression and inflammatory responses (Serebrovska et al., 2020).

328

329 At present there are limited therapeutic options for treating COVID-19 most of which treat the clinical  
330 manifestation of the disease. FG-4592 treatment before or after SARS-CoV-2 infection reduced the  
331 infectious viral burden and restored the loss of ciliated cells, providing an opportunity to improve  
332 clinical outcomes by limiting secondary infections. Our observations may be applicable for the  
333 treatment of other respiratory pathogens, including both Influenza A virus (Ren et al., 2019; Zhao et  
334 al., 2020) and Respiratory Syncytial virus, whose replication has been reported to be HIF-dependent  
335 (Morris et al., 2020). In summary, we demonstrate a role for HIFs to suppress SARS-CoV-2 infection  
336 and associated disease in an experimental animal model, highlighting the value of prolyl-hydroxylase  
337 inhibitors for the treatment of COVID-19.

338

## 339 **METHODS**

### 340 **Animals.**

341 Golden Syrian hamsters 9 (*Mesocricetus auratus*) aged 6–8 weeks were obtained from Envigo RMS  
342 UK Ltd., Bicester, UK. The animals were housed in cages that are designed in accordance with the  
343 requirements of the UK Home Office Code of Practice for the Housing and Care of Animal Used for  
344 Scientific Procedures (1986). During procedures with SARS-CoV-2, the animals were housed in a  
345 flexible-film isolator within a Containment Level 3 facility. The animals were randomly assigned into  
346 groups and individually housed, with equal allocation of male and female animals to each study. For  
347 direct intranasal challenge studies, group sizes of 6 hamsters were used as the minimal number  
348 required for statistical significance to be achieved. Access to food and water was ad libitum and  
349 environment enrichment was provided. Rooms were maintained within set parameters: 20–24 °C, 45–  
350 65% humidity and a 12/12 light cycle.

351

### 352 **Syrian Hamster study design and ethics approval.**

353 Animals were divided into three groups for treatment with vehicle, FG-4592 pre-infection or post-  
354 infection (n=6 per group). Animals were treated with 30mg/kg of FG-4592 (MedChem Express) by  
355 oral gavage. Drug was dissolved in 99% double distilled H<sub>2</sub>O, 0.5% methyl cellulase and 0.5%  
356 Tween-80, administered twice daily. Treatment commenced either 24h prior to (pre) or 24h following  
357 (post) infection and maintained until termination of the study (4 days) after infection. The control group  
358 followed the dosing schedule of the pre-infection group and were treated with vehicle only. All groups  
359 were infected intranasally with 5x10<sup>4</sup> PFU of Australia/VIC01/2020 SARS-CoV-2. Viral inocula were  
360 made in sterile phosphate buffered saline (PBS) and delivered via intranasal instillation (200µL total

361 with 100 $\mu$ L per nare) with animals sedated using isoflurane. Animal weights and temperatures were  
362 monitored daily and visual inspection of all animals carried out twice daily, with signs of clinical  
363 disease such as wasp waisted, ruffled fur, hunched or laboured breathing recorded (**Supplementary**  
364 **Table 1**). Throat swabs and nasal washes were collected on days 1, 2 and 4 post infection. Animals  
365 were euthanised at day 4 post infection and tissues collected at necropsy for pathology and virology  
366 assays. All experimental work was conducted under the authority of a UK Home Office approved  
367 project licence that had been subject to local ethical review at Public Health England (now part of the  
368 UK Health Security Agency (UKHSA) Porton Down by the Animal Welfare and Ethical Review Body  
369 (AWERB) as required by the Home Office Animals (Scientific Procedures) Act 1986.

370

371 **Virus and cells.**

372 SARS-CoV-2 Australia/VIC01/2020(Caly et al., 2020) was provided by the Peter Doherty Institute for  
373 Infection and Immunity, Melbourne, Australia at P1 and passaged twice in Vero/hSLAM cells  
374 (Cat#04091501) obtained from the European Collection of Cell Cultures (ECACC), UK. Virus  
375 infectivity was determined by plaque assay on Vero-TMPRSS2 cells as previously reported (Wing et  
376 al., 2021a). Calu-3 cells were obtained from Prof Nicole Zitzmann's lab and maintained in Advanced  
377 DMEM, 10% FCS, L-glutamine and penicillin streptomycin. Calu-3 cells were infected with the above  
378 strain of SARS-CoV-2 at an MOI of 0.01 for 2h. Viral inocula were removed, cells washed three times  
379 in PBS and maintained in growth media until harvest.

380

381 **Plaque assay quantification of virus infectivity.**

382 Samples from nasal washes, throat swabs or lung homogenates were serially diluted 1:10 and used  
383 to inoculate monolayers of Vero-TMPRSS2 cells for 2h. Inocula were removed and replaced with  
384 DMEM containing 1% FCS and a semi-solid overlay consisting of 1.5% carboxymethyl cellulose  
385 (SIGMA). Cells were incubated for 72h, after which cells were fixed in 4% PFA, stained with 0.2%  
386 crystal violet (w/v) and visible plaques enumerated.

387

388 **qPCR quantification.**

389 Viral RNA was extracted from nasal washes or throat swabs using the QiaAMP Viral RNA kit (Qiagen)  
390 according to manufacturer's instructions. Tissues were homogenised using the GentleMACS  
391 homogeniser in RLT buffer and extracted using the RNeasy kit (Qiagen) according to manufacturer's  
392 instructions. For quantification of viral or cellular RNA, equal amounts of RNA, as determined by  
393 nanodrop, were used in a one-step RT-qPCR using the Takyon-One Step RT probe mastermix  
394 (Eurogentec) and run on a Roche Light Cycler 96. For quantification of viral copy numbers, qPCR  
395 runs contained serial dilutions of viral RNA standards. Total SARS-CoV-2 RNA was quantified using:  
396 2019-nCoV\_N1-F: 5'-GAC CCC AAA ATC AGC GAA AT-3', 2019-nCoV\_N1-R: 5'-TCT GGT TAC  
397 TGC CAG TTG AA TCT G-3', 2019-nCoV\_N1-Probe: 5'-FAM-ACC CCG CAT TAC GTT TGG TGG  
398 ACC-BHQ1-3'. Genomic viral RNA was quantified using SARS-CoV-2-gRNA\_F: 5'- ACC AAC CAA  
399 CTT TCG ATC TCT TGT-3', SARS-CoV-2-gRNA\_R: 5'-CCT CCA CGG AGT CTC CAA AG-3', SARS-  
400 CoV-2-gRNA\_Probe: 5' FAM-GCT GGT AGT GAC TGC TTT TCG CCC C-BHQ1-3'. Hamster host

401 transcripts were quantified using the following Taqman expression assays by ThermoFisher, *Edn1*  
402 (APAAFZZ), *Ace2* (1956514) and *β-Actin* (APZTJRT).

403

404 **Histopathology, *in situ* hybridisation and Immunohistochemistry.**

405 The nasal cavity and left lung were fixed by immersion in 10% neutral-buffered formalin and  
406 processed into paraffin wax. Nasal cavity samples were decalcified using an EDTA-based solution  
407 prior to longitudinal sectioning to expose the respiratory and olfactory epithelium. Sequential 4 µm  
408 sections were stained with H&E. In addition, samples were stained using the *in-situ* hybridisation  
409 (ISH) RNAscope technique to label SARS-CoV-2 RNA using V-nCoV2019-S probe (Cat No. 848561,  
410 Advanced Cell Diagnostics). Briefly, tissues were pre-treated with hydrogen peroxide for 10 min (room  
411 temperature), target retrieval for 15 min (98–101°C) and protease plus for 30 min (40°C) (Advanced  
412 Cell Diagnostics). The probe was incubated with the tissues for 2h at 40°C and the signal amplified  
413 using RNAscope 2.5 HD Detection kit – Red (Advanced Cell Diagnostics). Immunohistochemical  
414 (IHC) staining of the SARS-CoV-2 nucleocapsid (N) protein, deparaffinisation and heat-induced  
415 epitope retrieval were performed on the Leica BOND-RXm using BOND Epitope Retrieval Solution 2  
416 (ER2, pH 9.0) for 30 minutes at 95°C. Staining was performed with the BOND Polymer Refine  
417 Detection kit, a rabbit anti-SARS-CoV-2 nucleocapsid antibody (Sinobiological; clone: #001; dilution:  
418 1:5000) and counterstained with haematoxylin. The H&E, ISH and IHC stained slides were scanned  
419 using a Hamamatsu S360 digital slide scanner and examined using ndp.view2 software (v2.8.24).  
420 Lung tissue from one animal in the vehicle group was not processed due to deterioration of the  
421 sample. Digital image analysis using Nikon NIS-Ar software quantified SARS-CoV-2 RNA or N  
422 expression in the lung sections by calculating the percentage of positively stained areas in defined  
423 regions of interest (ROI), including the airway epithelia and parenchyma. For the nasal cavity a semi-  
424 quantitative scoring system (Dowall et al., 2021) evaluated the presence of SARS-CoV-2 RNA or N  
425 expression in the exudate and epithelia where: 0=no staining; 1=minimal; 2=mild; 3=moderate and  
426 4=abundant staining. All slides were evaluated subjectively by a qualified pathologist, blinded to  
427 treatment details and were randomised prior to examination to limit bias (blind evaluation). Random  
428 slides were peer-reviewed by a second pathologist. Histopathology was carried out in a  
429 ISO9001:2015 and GLP compliant laboratory. A semiquantitative scoring system evaluated the  
430 severity of lesions in the lung and nasal cavity as previously reported (Dowall et al., 2021).

431

432 **RNA sequencing and data analysis.**

433 RNA was extracted from 30mg of homogenised lung (right lobe) using the RNeasy kit (Qiagen) and  
434 RNA integrity determined by Tapestation (Agilent), before providing RNA to Novogene UK Ltd for  
435 poly-A-enriched transcriptome sequencing. Paired end Illumina sequencing was carried out with  
436 a300bp fragment length and mapped to the *Mesocricetus auratus* genome. Viral reads were mapped  
437 to the SARS-CoV-2 reference genome (NC 045512.2) using Salmon (Patro et al., 2017). FPKM  
438 values were enumerated, and differential expression quantified using the DeSeq2 package (Love et  
439 al., 2014). Threshold for statistical significance was set as  $\log_2\text{FC} +/ - 1$  and an adjusted p value

440 <0.05. Junction spanning reads were detected as described in Kim et al 2021(Kim et al., 2020) using  
441 the ggsashimi analysis package (Love et al., 2014).

442

#### 443 **Immunoblotting.**

444 Cells were prepared by washing cells with PBS and lysed using RIPA buffer (20 mM Tris, pH 7.5, 2  
445 mM EDTA, 150 mM NaCl, 1% NP40, and 1% sodium deoxycholate) supplemented with protease  
446 inhibitor cocktail tablets (Roche). Clarified samples were mixed with laemmli sample buffer, separated  
447 by SDS-PAGE and proteins transferred to polyvinylidene difluoride membrane. Membranes were  
448 blocked in 5% milk in PBS/0.1% Tween-20 and incubated with anti-HIF-1 $\alpha$  (BD Biosciences), anti- $\beta$ -  
449 Actin (Sigma) or SARS-CoV-2 nucleocapsid (EY-2A, a kind gift from Prof Alain Townsend) primary  
450 antibodies and appropriate HRP-conjugated secondary antibodies (DAKO). Chemiluminescence  
451 substrate (West Dura, 34076, Thermo Fisher Scientific) was used to visualize proteins using a G:Box  
452 Imaging system (Syngene).

453

#### 454 **Visualising SARS-CoV-2 RNAs by Northern Blotting.**

455 Infected Calu-3 cells were harvested in Trizol (Thermofisher) 24h post infection and total RNA  
456 extracted according to manufacturer's instructions. 10  $\mu$ g of RNA was resolved on a 10% MOPS, 2.2  
457 M formaldehyde agarose gel. To show equal RNA loading, the 18S and 28S ribosomal subunit RNA  
458 species were visualised under UV light through ethidium bromide staining. Gels were denatured in 50  
459 mM NaOH for 5 minutes, and RNAs transferred to nylon membrane by capillary transfer in 1XSSC  
460 buffer. Membranes were washed and RNAs fixed by UV crosslinking. Membranes were hybridised at  
461 65°C overnight with a digoxigenin-labelled DNA probe specific to the 3' end of the SARS-CoV-2  
462 genome, enabling the detection of all viral RNAs. Bands were visualised using a luminescent DIG  
463 detection kit (Roche) according to manufacturer's instructions.

464

#### 465 **Statistical Analysis.**

466 All data are presented as mean values  $\pm$  SEM. P values were determined using the Mann-Whitney  
467 test (two group comparisons) or with the Kruskal-Wallis ANOVA (multi group comparisons) using  
468 PRISM version 8. In the figures \* denotes p < 0.05, \*\* < 0.01, \*\*\* <0.001 and \*\*\*\* <0.0001.

469

#### 470 **Data availability.**

471 The authors declare that all data supporting the findings of this study are available within the article  
472 and its Supplementary Information files or are available from the authors upon request. RNAseq data  
473 from this study are deposited on NCBI under the GEO accession ID: GSE195879  
474 (<https://www.ncbi.nlm.nih.gov/geo/query/acc.cgi?acc=GSE195879>)

475

#### 476 **ACKNOWLEDGEMENTS.**

477 The authors would like to thank our colleagues at the University of Oxford, Anderson Ryan and Nicole  
478 Zitzmann for Calu-3 cells, William James for Vero-E6 TMPRSS2 and Alain Townsend for anti-  
479 nucleocapsid. We acknowledge the support from the Biological Investigations Group and

480 Histopathology Department at the UK Health Security Agency, Porton Down. JAM is funded by a  
481 Wellcome Investigator Award 200838/Z/16/Z, UK Medical Research Council (MRC) project grant  
482 MR/R022011/1 and Chinese Academy of Medical Sciences (CAMS) Innovation Fund for Medical  
483 Science (CIFMS), China (grant number: 2018-I2M-2-002). FI is funded by the Wellcome Trust  
484 211122/Z/18 and AC is supported by an Oxford-BMS Fellowship. TB is funded by the Paradifference  
485 Foundation and COVID-19 Research Response Fund, University of Oxford. SC and AW are funded  
486 by the Francis Crick Institute, which receives its core funding from Cancer Research UK (FC001206),  
487 the UK Medical Research Council (FC001206), and the Wellcome Trust (FC001206).

488

489 **AUTHOR CONTRIBUTIONS.**

490 PACW designed and conducted experiments and co-wrote MS; MPB designed and conducted  
491 experiments; AC designed and conducted experiments; SC designed and conducted experiments;  
492 COR provided technical help; XC conducted experiments; JMH analysed data; XZ conducted  
493 experiments; RLJ performed experiments; KAR performed experiments; YH co-designed the study;;  
494 MWC helped with study design;; FI advised on tissue staining;; PB analysed data;; AW designed  
495 experiments and co-wrote MS; TB co-designed the study and co-wrote MS; FJS analysed data and  
496 co-wrote MS; JAM designed the study and co-wrote MS.

497

498 **DECLARATION OF INTERESTS.**

499 The other authors declare no financial interests.

500

501

502 **FIGURE LEGENDS**

503 **Figure 1: Evaluating FG-4592 in the Syrian hamster model of SARS-CoV-2.**

504 **(A)** Schematic of the challenge study. 18 animals aged 7 weeks were allocated into groups of 6 for  
505 each treatment. For vehicle and pre-infection groups, twice daily dosing of vehicle or 30mg/kg of FG-  
506 4592 administered by oral gavage commenced 24h prior to intranasal challenge with SARS-CoV-2  
507 VIC01/2020 (5x10<sup>4</sup> PFU). For the post-infection treatment group, FG-4592 dosing started 24h after  
508 viral infection. On days 1, 2 and 4 post-infection, nasal washes and throat swabs were collected for  
509 assessment of viral load and infectious titre. The study was terminated at 4 days post-infection. **(B)**  
510 Hamster temperature and weight measurements over the course of the study. Weights were  
511 measured daily, and temperature recorded twice daily with average measurements for each animal  
512 plotted. **(C)** Clinical scores from daily animal assessments across the treatment groups. Observations  
513 such as wasp waisted, ruffled fur, hunched or laboured breathing were recorded and assigned a  
514 numerical value (see **Supplementary Table 1**). **(D)** Reticulocyte counts were quantified by staining  
515 terminal blood samples with 0.1% Brilliant Cresyl Blue. Endothelin-1 (*Edn1*) **(E)** and Ace2 **(F)** mRNA  
516 levels in the lung and data expressed relative to the mean of the control Vehicle group. Open circles  
517 represent female animals and closed circles males. Unless otherwise stated, data is expressed as  
518 mean  $\pm$  s.d. Statistical analysis was performed using a one-way ANOVA, p<0.05 = \*, p<0.01 = \*\*,  
519 p<0.001 = \*\*\*.

520

521 **Figure 2: FG-4592 treatment reduces the infectious SARS-CoV-2 burden in the respiratory**  
522 **tract.**

523 **(A)** The infectious burden in the nasal washes sampled at days 1, 2, and 4 post-infection was  
524 quantified by plaque assay on Vero-TMPRSS2 cells and data presented as plaque forming units  
525 (PFU) per ml. Viral RNA copies were measured by RT-qPCR and expressed as copies/mL. **(B)** Viral  
526 infectivity and RNA copies were measured in throat swabs as described above. **(C)** Snap frozen lung  
527 samples from the right lobe harvested at termination were homogenised for RNA extraction and  
528 titration of infectious virus. Viral RNA copies were quantified by RT-qPCR and expressed as  
529 copies/µg of total RNA. Infectious titre was determined by plaque assay and expressed as PFU/mg of  
530 lung tissue. Open circles represent female animals and closed circles males. Statistical analysis was  
531 performed by ANOVA,  $p<0.05 = ^*$ ,  $p<0.01 = ^{**}$ ,  $p<0.0001 = ^{***}$ ,  $p<0.0001 = ^{****}$ . Brackets indicate the  
532 comparisons tested.

533

534 **Figure 3: Analysis of the SARS-CoV-2 transcriptome in FG-4592 treated hamster lung and in**  
535 **Calu-3 cells.** **(A)** Viral sequencing reads from infected lung tissue were mapped to the SARS-CoV-2  
536 Victoria reference genome to generate a read depth profile. Reads that spanned the canonical viral  
537 sub-genomic transcript junctions were quantified for each tissue sample. **(B)** Junction spanning reads  
538 quantified from control or FG-4592 (50µM) pre-treated Calu-3 cells infected with SARS-CoV-2 (MOI of  
539 0.01) (N=3 biological replicates). **(C)** Viral RNAs from the experiment in (B) were resolved on an RNA-  
540 agarose gel and analysed by Northern Blot hybridisation using a dioxygenin labelled probe designed  
541 to detect all viral transcripts. Relative expression of transcripts was determined by densitometric  
542 analysis relative to the 28S/18S ribosomal RNA. **(D)** Representative immunoblot of SARS-CoV-2  
543 nucleocapsid (N) and HIF-1 $\alpha$  expression in Calu-3 cells treated with FG-4592 (25 or 50µM) pre- or  
544 post- infection. N expression was quantified by densitometry relative to  $\beta$ -actin and data expressed  
545 relative to the vehicle control. Statistical analysis was performed by ANOVA,  $p<0.05 = ^*$ ,  $p<0.0001 =$   
546  $^{****}$ . Brackets indicate the comparisons tested.

547

548 **Figure 4: SARS-CoV-2 RNA and pathology in the nasal tract and lung.**

549 **(A)** Sections from the left lung and nasal cavity were stained with H&E to analyse histopathological  
550 changes and with RNA *in-situ* hybridisation (ISH) to detect SARS-CoV-2 RNA using probes specific  
551 for the viral Spike (S) transcript. Representative images from each treatment group are shown. Lung  
552 lesions consisted of multifocal broncho-interstitial pneumonia (\*) with mild to moderate necrosis of the  
553 bronchiolar epithelium (arrows and H&E inserts) (see **Supplementary Fig.5**). ISH shows abundant  
554 viral RNA in the nasal cavity epithelia that associates with mild to moderate necrosis (inserts) and  
555 within the airway epithelia and areas of inflammation. Scale bar = 100µm. **(B)** Nasal cavity was  
556 assessed for the presence and severity of lesions using a semi-quantitative scoring system from  
557 H&E-stained sections. SARS-CoV-2 RNA in the olfactory epithelium or exudates was quantified using  
558 the following scoring system: 0=no positive staining; 1=minimal; 2=mild; 3=moderate and 4=abundant  
559 staining. **(C)** Lung pathology was assessed for the presence and severity of lesions using a semi-

560 quantitative scoring system from H&E-stained sections. Digital image analysis calculated the area of  
561 lung airway and parenchyma staining for viral RNA. Statistical analysis was performed using a one-  
562 way ANOVA,  $p<0.05 = ^*$ ,  $p<0.01 = ^{**}$ . N=5 animals for vehicle and N=6 animals for each treatment  
563 group.

564

565 **Figure 5: SARS-CoV-2 nucleocapsid expression in the nasal tract and lung.**

566 **(A)** Sections from the nasal cavity were stained by immunohistochemistry for the presence of the  
567 SARS-CoV-2 N protein. Representative images from each treatment group are displayed. N protein  
568 staining was observed in the olfactory epithelia (ep) and the inflammatory exudates (ex) within the  
569 nasal cavity luminae. Bar = 50 $\mu$ m. **(B)** A semiquantitative scoring system evaluated N protein  
570 expression in the olfactory epithelia or exudates, where: 0=no positive staining; 1=minimal; 2=mild;  
571 3=moderate and 4=abundant staining. **(C)** Lung sections were assessed for N protein expression and  
572 representative images show positive staining in the bronchiolar epithelia, luminae (br) together and  
573 parenchyma (p). **(D)** Digital image analysis calculated the area of lung airway and parenchyma  
574 staining for N protein. Statistical analysis was performed by ANOVA,  $p<0.05 = ^*$ ,  $p<0.01 = ^{**}$ . N=5  
575 animals for vehicle and N=6 animals for each treatment group.

576

577 **Figure 6: SARS-CoV-2 driven changes in lung ciliated epithelia.**

578 **(A)** RNA extracted from snap frozen lung tissue from, vehicle (N=5), FG-4592 treated pre- (N=6) and  
579 post-infection (N=6), or uninfected animals (N=2) was sequenced. Differential gene expression,  
580 defined as a  $\log_2$  fold change of +/- 1 with an adjusted p value <0.05, was measured for the SARS-  
581 CoV-2 infected vehicle and uninfected samples. **(B)** Significant gene ontology pathways are displayed  
582 for both up and down regulated genes in infected vehicle vs uninfected samples, where symbol size  
583 reflects the -log10 adjusted p value and gene count is represented by the colour. **(C)** Expression of  
584 differentially expressed cilia-related genes, in vehicle, pre- and post-treatment groups compared to  
585 uninfected samples. Expression data is grouped by hierarchical clustering. **(D)**  $\log_2$  fold change  
586 values for all genes represented in C and grouped by treatment. Statistical analysis was performed  
587 using a one-way ANOVA, \*\*\* =  $p<0.001$ . **(E)** Representative lung sections stained for  $\alpha$ -tubulin or  
588 CCSP from uninfected, vehicle, FG-4592 pre-or post-infection treated animals where nuclei are  
589 visualised with DAPI. Individual stains are shown along with an overlayed image. Scale bars  
590 represent

100 $\mu$ m.

591

592

593

594

595

## REFERENCES

596

597 Akizawa, T., Iwasaki, M., Yamaguchi, Y., Majikawa, Y., and Reusch, M. (2020a). Phase 3,  
598 Randomized, Double-Blind, Active-Comparator (Darbepoetin Alfa) Study of Oral Roxadustat in CKD  
599 Patients with Anemia on Hemodialysis in Japan. *J Am Soc Nephrol* 31, 1628-1639.

600 Akizawa, T., Nangaku, M., Yonekawa, T., Okuda, N., Kawamatsu, S., Onoue, T., Endo, Y., Hara, K.,  
601 and Cobitz, A.R. (2020b). Efficacy and Safety of Daprodustat Compared with Darbepoetin Alfa in  
602 Japanese Hemodialysis Patients with Anemia: A Randomized, Double-Blind, Phase 3 Trial. *Clin J Am  
603 Soc Nephrol* 15, 1155-1165.

604 Akizawa, T., Otsuka, T., Reusch, M., and Ueno, M. (2020c). Intermittent Oral Dosing of Roxadustat in  
605 Peritoneal Dialysis Chronic Kidney Disease Patients with Anemia: A Randomized, Phase 3,  
606 Multicenter, Open-Label Study. *Ther Apher Dial* 24, 115-125.

607 Akizawa, T., Yamaguchi, Y., Otsuka, T., and Reusch, M. (2020d). A Phase 3, Multicenter,  
608 Randomized, Two-Arm, Open-Label Study of Intermittent Oral Dosing of Roxadustat for the  
609 Treatment of Anemia in Japanese Erythropoiesis-Stimulating Agent-Naive Chronic Kidney Disease  
610 Patients Not on Dialysis. *Nephron* 144, 372-382.

611 Alanio, A., Delliere, S., Fodil, S., Bretagne, S., and Megarbane, B. (2020). Prevalence of putative  
612 invasive pulmonary aspergillosis in critically ill patients with COVID-19. *Lancet Respir Med* 8, e48-  
613 e49.

614 Caly, L., Druce, J., Roberts, J., Bond, K., Tran, T., Kostecki, R., Yoga, Y., Naughton, W., Taiaroa, G.,  
615 Seemann, T., et al. (2020). Isolation and rapid sharing of the 2019 novel coronavirus (SARS-CoV-2)  
616 from the first patient diagnosed with COVID-19 in Australia. *Med J Aust* 212, 459-462.

617 Cevik, M., Tate, M., Lloyd, O., Maraolo, A.E., Schafers, J., and Ho, A. (2021). SARS-CoV-2, SARS-  
618 CoV, and MERS-CoV viral load dynamics, duration of viral shedding, and infectiousness: a systematic  
619 review and meta-analysis. *Lancet Microbe* 2, e13-e22.

620 Chan, J.F., Zhang, A.J., Yuan, S., Poon, V.K., Chan, C.C., Lee, A.C., Chan, W.M., Fan, Z., Tsoi,  
621 H.W., Wen, L., et al. (2020). Simulation of the Clinical and Pathological Manifestations of Coronavirus  
622 Disease 2019 (COVID-19) in a Golden Syrian Hamster Model: Implications for Disease Pathogenesis  
623 and Transmissibility. *Clin Infect Dis* 71, 2428-2446.

624 Chan, M.C., Ilott, N.E., Schodel, J., Sims, D., Tumber, A., Lipli, K., Mole, D.R., Pugh, C.W., Ratcliffe,  
625 P.J., Ponting, C.P., et al. (2016). Tuning the Transcriptional Response to Hypoxia by Inhibiting  
626 Hypoxia-inducible Factor (HIF) Prolyl and Asparaginyl Hydroxylases. *J Biol Chem* 291, 20661-20673.

627 Chen, N., Hao, C., Liu, B.C., Lin, H., Wang, C., Xing, C., Liang, X., Jiang, G., Liu, Z., Li, X., et al.  
628 (2019a). Roxadustat Treatment for Anemia in Patients Undergoing Long-Term Dialysis. *N Engl J Med*  
629 381, 1011-1022.

630 Chen, N., Hao, C., Peng, X., Lin, H., Yin, A., Hao, L., Tao, Y., Liang, X., Liu, Z., Xing, C., et al.  
631 (2019b). Roxadustat for Anemia in Patients with Kidney Disease Not Receiving Dialysis. *N Engl J  
632 Med* 381, 1001-1010.

633 Cross, A.R., de Andrea, C.E., María, V.-E., Landecho Acha, M.F., Cerundolo, L., Weeratunga, P.,  
634 Etherington, R., Denney, L., Ogg, G., Ho, L.P., et al. (2021). Spatial transcriptomic characterization of  
635 COVID-19 pneumonitis identifies immune circuits related to tissue injury  
636 . *BioRxiv*.

637 de Melo, G.D., Lazarini, F., Levallois, S., Hautefort, C., Michel, V., Larrous, F., Verillaud, B., Aparicio,  
638 C., Wagner, S., Gheusi, G., et al. (2021). COVID-19-related anosmia is associated with viral  
639 persistence and inflammation in human olfactory epithelium and brain infection in hamsters. *Sci  
640 Transl Med*.

641 Dejnirattisai, W., Huo, J., Zhou, D., Zahradník, J., Supasa, P., Liu, C., Duyvesteyn, H.M.E., Ginn,  
642 H.M., Mentzer, A.J., Tuekprakhon, A., *et al.* (2021a). Omicron-B.1.1.529 leads to widespread escape  
643 from neutralizing antibody responses. *bioRxiv*.

644 Dejnirattisai, W., Shaw, R.H., Supasa, P., Liu, C., Stuart, A.S., Pollard, A.J., Liu, X., Lambe, T., Crook,  
645 D., Stuart, D.I., *et al.* (2021b). Reduced neutralisation of SARS-CoV-2 omicron B.1.1.529 variant by  
646 post-immunisation serum. *Lancet*.

647 Dowall, S., Salguero, F.J., Wiblin, N., Fotheringham, S., Hatch, G., Parks, S., Gowan, K., Harris, D.,  
648 Carnell, O., Fell, R., *et al.* (2021). Development of a Hamster Natural Transmission Model of SARS-  
649 CoV-2 Infection. *Viruses* 13.

650 Gruber, A.D., Osterrieder, N., Bertzbach, L.D., Vladimirova, D., Greuel, S., Ihlow, J., Horst, D.,  
651 Trimpert, J., and Dietert, K. (2020). Standardization of Reporting Criteria for Lung Pathology in SARS-  
652 CoV-2-infected Hamsters: What Matters? *Am J Respir Cell Mol Biol* 63, 856-859.

653 Gualdoni, G.A., Mayer, K.A., Kapsch, A.M., Kreuzberg, K., Puck, A., Kienzl, P., Oberndorfer, F.,  
654 Fruhwirth, K., Winkler, S., Blaas, D., *et al.* (2018). Rhinovirus induces an anabolic reprogramming in  
655 host cell metabolism essential for viral replication. *Proc Natl Acad Sci U S A* 115, E7158-E7165.

656 Haeberle, H.A., Durrstein, C., Rosenberger, P., Hosakote, Y.M., Kuhlicke, J., Kempf, V.A., Garofalo,  
657 R.P., and Eltzschig, H.K. (2008). Oxygen-independent stabilization of hypoxia inducible factor (HIF)-1  
658 during RSV infection. *PLoS One* 3, e3352.

659 Hickey, M.M., Richardson, T., Wang, T., Mosqueira, M., Arguiri, E., Yu, H., Yu, Q.C., Solomides, C.C.,  
660 Morrisey, E.E., Khurana, T.S., *et al.* (2010). The von Hippel-Lindau Chuvash mutation promotes  
661 pulmonary hypertension and fibrosis in mice. *J Clin Invest* 120, 827-839.

662 Hiscox, J.A., Khoo, S.H., Stewart, J.P., and Owen, A. (2021). Shutting the gate before the horse has  
663 bolted: is it time for a conversation about SARS-CoV-2 and antiviral drug resistance? *J Antimicrob  
664 Chemother* 76, 2230-2233.

665 Hou, Y.J., Okuda, K., Edwards, C.E., Martinez, D.R., Asakura, T., Dinnon, K.H., 3rd, Kato, T., Lee,  
666 R.E., Yount, B.L., Mascenik, T.M., *et al.* (2020). SARS-CoV-2 Reverse Genetics Reveals a Variable  
667 Infection Gradient in the Respiratory Tract. *Cell* 182, 429-446 e414.

668 Huang, C., Wang, Y., Li, X., Ren, L., Zhao, J., Hu, Y., Zhang, L., Fan, G., Xu, J., Gu, X., *et al.* (2020).  
669 Clinical features of patients infected with 2019 novel coronavirus in Wuhan, China. *Lancet* 395, 497-  
670 506.

671 Huo, J., Mikolajek, H., Le Bas, A., Clark, J.J., Sharma, P., Kipar, A., Dormon, J., Norman, C.,  
672 Weckener, M., Clare, D.K., *et al.* (2021). A potent SARS-CoV-2 neutralising nanobody shows  
673 therapeutic efficacy in the Syrian golden hamster model of COVID-19. *Nat Commun* 12, 5469.

674 Huston, N.C., Wan, H., Strine, M.S., de Cesaris Araujo Tavares, R., Wilen, C.B., and Pyle, A.M.  
675 (2021). Comprehensive in vivo secondary structure of the SARS-CoV-2 genome reveals novel  
676 regulatory motifs and mechanisms. *Mol Cell* 81, 584-598 e585.

677 Imai, M., Iwatsuki-Horimoto, K., Hatta, M., Loeber, S., Halfmann, P.J., Nakajima, N., Watanabe, T.,  
678 Ujie, M., Takahashi, K., Ito, M., *et al.* (2020). Syrian hamsters as a small animal model for SARS-  
679 CoV-2 infection and countermeasure development. *Proc Natl Acad Sci U S A* 117, 16587-16595.

680 Jiang, J.H., Wang, N., Li, A., Liao, W.T., Pan, Z.G., Mai, S.J., Li, D.J., Zeng, M.S., Wen, J.M., and  
681 Zeng, Y.X. (2006). Hypoxia can contribute to the induction of the Epstein-Barr virus (EBV) lytic cycle.  
682 *J Clin Virol* 37, 98-103.

683 Kaelin, W.G., Jr., and Ratcliffe, P.J. (2008). Oxygen sensing by metazoans: the central role of the HIF  
684 hydroxylase pathway. *Mol Cell* 30, 393-402.

685 Kim, D., Lee, J.Y., Yang, J.S., Kim, J.W., Kim, V.N., and Chang, H. (2020). The Architecture of SARS-  
686 CoV-2 Transcriptome. *Cell* 181, 914-921 e910.

687 Kraus, R.J., Yu, X., Cordes, B.A., Sathiamoorthi, S., Iempridee, T., Nawandar, D.M., Ma, S., Romero-  
688 Masters, J.C., McChesney, K.G., Lin, Z., *et al.* (2017). Hypoxia-inducible factor-1alpha plays roles in  
689 Epstein-Barr virus's natural life cycle and tumorigenesis by inducing lytic infection through direct  
690 binding to the immediate-early BZLF1 gene promoter. *PLoS Pathog* 13, e1006404.

691 La Scola, B., Le Bideau, M., Andreani, J., Hoang, V.T., Grimaldier, C., Colson, P., Gautret, P., and  
692 Raoult, D. (2020). Viral RNA load as determined by cell culture as a management tool for discharge of  
693 SARS-CoV-2 patients from infectious disease wards. *Eur J Clin Microbiol Infect Dis* 39, 1059-1061.

694 Li, X., Xu, S., Yu, M., Wang, K., Tao, Y., Zhou, Y., Shi, J., Zhou, M., Wu, B., Yang, Z., *et al.* (2020).  
695 Risk factors for severity and mortality in adult COVID-19 inpatients in Wuhan. *J Allergy Clin Immunol*  
696 146, 110-118.

697 Liberzon, A., Birger, C., Thorvaldsdottir, H., Ghandi, M., Mesirov, J.P., and Tamayo, P. (2015). The  
698 Molecular Signatures Database (MSigDB) hallmark gene set collection. *Cell Syst* 1, 417-425.

699 Liu, C., Ginn, H.M., Dejnirattisai, W., Supasa, P., Wang, B., Tuekprakhon, A., Nutalai, R., Zhou, D.,  
700 Mentzer, A.J., Zhao, Y., *et al.* (2021). Reduced neutralization of SARS-CoV-2 B.1.617 by vaccine and  
701 convalescent serum. *Cell* 184, 4220-4236.e4213.

702 Liu, P.J., Balfe, P., McKeating, J.A., and Schilling, M. (2020). Oxygen Sensing and Viral Replication:  
703 Implications for Tropism and Pathogenesis. *Viruses* 12.

704 Love, M.I., Huber, W., and Anders, S. (2014). Moderated estimation of fold change and dispersion for  
705 RNA-seq data with DESeq2. *Genome Biol* 15, 550.

706 Manohar, P., Loh, B., Nachimuthu, R., Hua, X., Welburn, S.C., and Leptihn, S. (2020). Secondary  
707 Bacterial Infections in Patients With Viral Pneumonia. *Front Med (Lausanne)* 7, 420.

708 Morris, D.R., Qu, Y., Agrawal, A., Garofalo, R.P., and Casola, A. (2020). HIF-1alpha Modulates Core  
709 Metabolism and Virus Replication in Primary Airway Epithelial Cells Infected with Respiratory  
710 Syncytial Virus. *Viruses* 12.

711 Moser, S.C., Bensaddek, D., Ortmann, B., Maure, J.F., Mudie, S., Blow, J.J., Lamond, A.I., Swedlow,  
712 J.R., and Rocha, S. (2013). PHD1 links cell-cycle progression to oxygen sensing through  
713 hydroxylation of the centrosomal protein Cep192. *Dev Cell* 26, 381-392.

714 Nouailles, G., Wyler, E., Pennitz, P., Postmus, D., Vladimirova, D., Kazmierski, J., Pott, F., Dietert, K.,  
715 Muelleder, M., Farztdinov, V., *et al.* (2021). Temporal omics analysis in Syrian hamsters unravel  
716 cellular effector responses to moderate COVID-19. *Nat Commun* 12, 4869.

717 Owen, D.R., Allerton, C.M.N., Anderson, A.S., Aschenbrenner, L., Avery, M., Berritt, S., Boras, B.,  
718 Cardin, R.D., Carlo, A., Coffman, K.J., *et al.* (2021). An oral SARS-CoV-2 M(pro) inhibitor clinical  
719 candidate for the treatment of COVID-19. *Science* 374, 1586-1593.

720 Page, L.K., Staples, K.J., Spalluto, C.M., Watson, A., and Wilkinson, T.M.A. (2021). Influence of  
721 Hypoxia on the Epithelial-Pathogen Interactions in the Lung: Implications for Respiratory Disease.  
722 *Front Immunol* 12, 653969.

723 Palazon, A., Goldrath, A.W., Nizet, V., and Johnson, R.S. (2014). HIF transcription factors,  
724 inflammation, and immunity. *Immunity* 41, 518-528.

725 Patro, R., Duggal, G., Love, M.I., Irizarry, R.A., and Kingsford, C. (2017). Salmon provides fast and  
726 bias-aware quantification of transcript expression. *Nat Methods* 14, 417-419.

727 Pizzorno, A., Padey, B., Julien, T., Trouillet-Assant, S., Traversier, A., Errazuriz-Cerda, E., Fouret, J.,  
728 Dubois, J., Gaymard, A., Lescure, F.X., *et al.* (2020). Characterization and Treatment of SARS-CoV-2  
729 in Nasal and Bronchial Human Airway Epithelia. *Cell Rep Med* 1, 100059.

730 Polke, M., Seiler, F., Lepper, P.M., Kamyschnikow, A., Langer, F., Monz, D., Herr, C., Bals, R., and  
731 Beisswenger, C. (2017). Hypoxia and the hypoxia-regulated transcription factor HIF-1alpha suppress  
732 the host defence of airway epithelial cells. *Innate Immun* 23, 373-380.

733 Provenzano, R., Besarab, A., Sun, C.H., Diamond, S.A., Durham, J.H., Cangiano, J.L., Aiello, J.R.,  
734 Novak, J.E., Lee, T., Leong, R., *et al.* (2016). Oral Hypoxia-Inducible Factor Prolyl Hydroxylase  
735 Inhibitor Roxadustat (FG-4592) for the Treatment of Anemia in Patients with CKD. *Clin J Am Soc  
736 Nephrol* 11, 982-991.

737 Ren, L., Zhang, W., Han, P., Zhang, J., Zhu, Y., Meng, X., Zhang, J., Hu, Y., Yi, Z., and Wang, R.  
738 (2019). Influenza A virus (H1N1) triggers a hypoxic response by stabilizing hypoxia-inducible factor-  
739 1alpha via inhibition of proteasome. *Virology* 530, 51-58.

740 Robinot, R., Hubert, M., de Melo, G.D., Lazarini, F., Bruel, T., Smith, N., Levallois, S., Larrous, F.,  
741 Fernandes, J., Gellenoncourt, S., *et al.* (2021). SARS-CoV-2 infection induces the dedifferentiation of  
742 multiciliated cells and impairs mucociliary clearance. *Nat Commun* 12, 4354.

743 Rosenke, K., Hansen, F., Schwarz, B., Feldmann, F., Haddock, E., Rosenke, R., Barbian, K., Meade-  
744 White, K., Okumura, A., Leventhal, S., *et al.* (2021). Orally delivered MK-4482 inhibits SARS-CoV-2  
745 replication in the Syrian hamster model. *Nat Commun* 12, 2295.

746 Rosenke, K., Meade-White, K., Letko, M., Clancy, C., Hansen, F., Liu, Y., Okumura, A., Tang-Huau,  
747 T.L., Li, R., Saturday, G., *et al.* (2020). Defining the Syrian hamster as a highly susceptible preclinical  
748 model for SARS-CoV-2 infection. *Emerg Microbes Infect* 9, 2673-2684.

749 Ryan, K.A., Watson, R.J., Bewley, K.R., Burton, C., Carnell, O., Cavell, B.E., Challis, A., Coombes,  
750 N.S., Emery, K., Fell, R., *et al.* (2021). Convalescence from prototype SARS-CoV-2 protects Syrian  
751 hamsters from disease caused by the Omicron variant. *bioRxiv*, 2021.2012.2024.474081.

752 Sampaio, N.G., Chauveau, L., Hertzog, J., Bridgeman, A., Fowler, G., Moonen, J.P., Dupont, M.,  
753 Russell, R.A., Noerenberg, M., and Rehwinkel, J. (2021). The RNA sensor MDA5 detects SARS-CoV-  
754 2 infection. *Sci Rep* 11, 13638.

755 Schley, G., Klanke, B., Kalucka, J., Schatz, V., Daniel, C., Mayer, M., Goppelt-Struebe, M., Herrmann,  
756 M., Thorsteinsdottir, M., Palsson, R., *et al.* (2019). Mononuclear phagocytes orchestrate prolyl  
757 hydroxylase inhibition-mediated renoprotection in chronic tubulointerstitial nephritis. *Kidney Int* 96,  
758 378-396.

759 Schodel, J., Oikonomopoulos, S., Ragoussis, J., Pugh, C.W., Ratcliffe, P.J., and Mole, D.R. (2011).  
760 High-resolution genome-wide mapping of HIF-binding sites by ChIP-seq. *Blood* 117, e207-217.

761 Semenza, G.L. (2011). Regulation of metabolism by hypoxia-inducible factor 1. *Cold Spring Harb  
762 Symp Quant Biol* 76, 347-353.

763 Serebrovska, Z.O., Chong, E.Y., Serebrovska, T.V., Tumanovska, L.V., and Xi, L. (2020). Hypoxia,  
764 HIF-1alpha, and COVID-19: from pathogenic factors to potential therapeutic targets. *Acta Pharmacol  
765 Sin* 41, 1539-1546.

766 Sia, S.F., Yan, L.M., Chin, A.W.H., Fung, K., Choy, K.T., Wong, A.Y.L., Kaewpreedee, P., Perera, R.,  
767 Poon, L.L.M., Nicholls, J.M., *et al.* (2020). Pathogenesis and transmission of SARS-CoV-2 in golden  
768 hamsters. *Nature* 583, 834-838.

769 Simmonds, P., Williams, S., and Harvala, H. (2021). Understanding the outcomes of COVID-19 - does  
770 the current model of an acute respiratory infection really fit? *J Gen Virol* 102.

771 Singanayagam, A., Hakki, S., Dunning, J., Madon, K.J., Crone, M.A., Koycheva, A., Derqui-  
772 Fernandez, N., Barnett, J.L., Whitfield, M.G., Varro, R., *et al.* (2021). Community transmission and  
773 viral load kinetics of the SARS-CoV-2 delta (B.1.617.2) variant in vaccinated and unvaccinated  
774 individuals in the UK: a prospective, longitudinal, cohort study. *Lancet Infect Dis.*

775 Sposito, B., Broggi, A., Pandolfi, L., Crotta, S., Clementi, N., Ferrarese, R., Sisti, S., Criscuolo, E.,  
776 Spreafico, R., Long, J.M., *et al.* (2021). The interferon landscape along the respiratory tract impacts  
777 the severity of COVID-19. *Cell* 184, 4953-4968 e4916.

778 Urrutia, A.A., and Aragones, J. (2018). HIF Oxygen Sensing Pathways in Lung Biology. *Biomedicines*  
779 6.

780 van Dam, T.J.P., Kennedy, J., van der Lee, R., de Vrieze, E., Wunderlich, K.A., Rix, S., Dougherty,  
781 G.W., Lambacher, N.J., Li, C., Jensen, V.L., *et al.* (2019). CiliaCarta: An integrated and validated  
782 compendium of ciliary genes. *PLoS One* 14, e0216705.

783 Voysey, M., Clemens, S.A.C., Madhi, S.A., Weckx, L.Y., Folegatti, P.M., Aley, P.K., Angus, B., Baillie,  
784 V.L., Barnabas, S.L., Bhorat, Q.E., *et al.* (2021). Safety and efficacy of the ChAdOx1 nCoV-19  
785 vaccine (AZD1222) against SARS-CoV-2: an interim analysis of four randomised controlled trials in  
786 Brazil, South Africa, and the UK. *Lancet* 397, 99-111.

787 Walsh, K.A., Jordan, K., Clyne, B., Rohde, D., Drummond, L., Byrne, P., Ahern, S., Carty, P.G.,  
788 O'Brien, K.K., O'Murchu, E., *et al.* (2020). SARS-CoV-2 detection, viral load and infectivity over the  
789 course of an infection. *J Infect* 81, 357-371.

790 Wing, P.A.C., Keeley, T.P., Zhuang, X., Lee, J.Y., Prange-Barczynska, M., Tsukuda, S., Morgan,  
791 S.B., Harding, A.C., Argles, I.L.A., Kurlekar, S., *et al.* (2021a). Hypoxic and pharmacological activation  
792 of HIF inhibits SARS-CoV-2 infection of lung epithelial cells. *Cell Rep* 35, 109020.

793 Wing, P.A.C., Liu, P.J., Harris, J.M., Magri, A., Michler, T., Zhuang, X., Borrman, H., Minisini, R.,  
794 Frampton, N.R., Wetten, J.M., *et al.* (2021b). Hypoxia inducible factors regulate hepatitis B virus  
795 replication by activating the basal core promoter. *J Hepatol.*

796 Zhao, C., Chen, J., Cheng, L., Xu, K., Yang, Y., and Su, X. (2020). Deficiency of HIF-1alpha  
797 enhances influenza A virus replication by promoting autophagy in alveolar type II epithelial cells.  
798 *Emerg Microbes Infect* 9, 691-706.

799 Zhu, N., Wang, W., Liu, Z., Liang, C., Wang, W., Ye, F., Huang, B., Zhao, L., Wang, H., Zhou, W., *et*  
800 *al.* (2020). Morphogenesis and cytopathic effect of SARS-CoV-2 infection in human airway epithelial  
801 cells. *Nat Commun* 11, 3910.

802

803

**Figure 1**

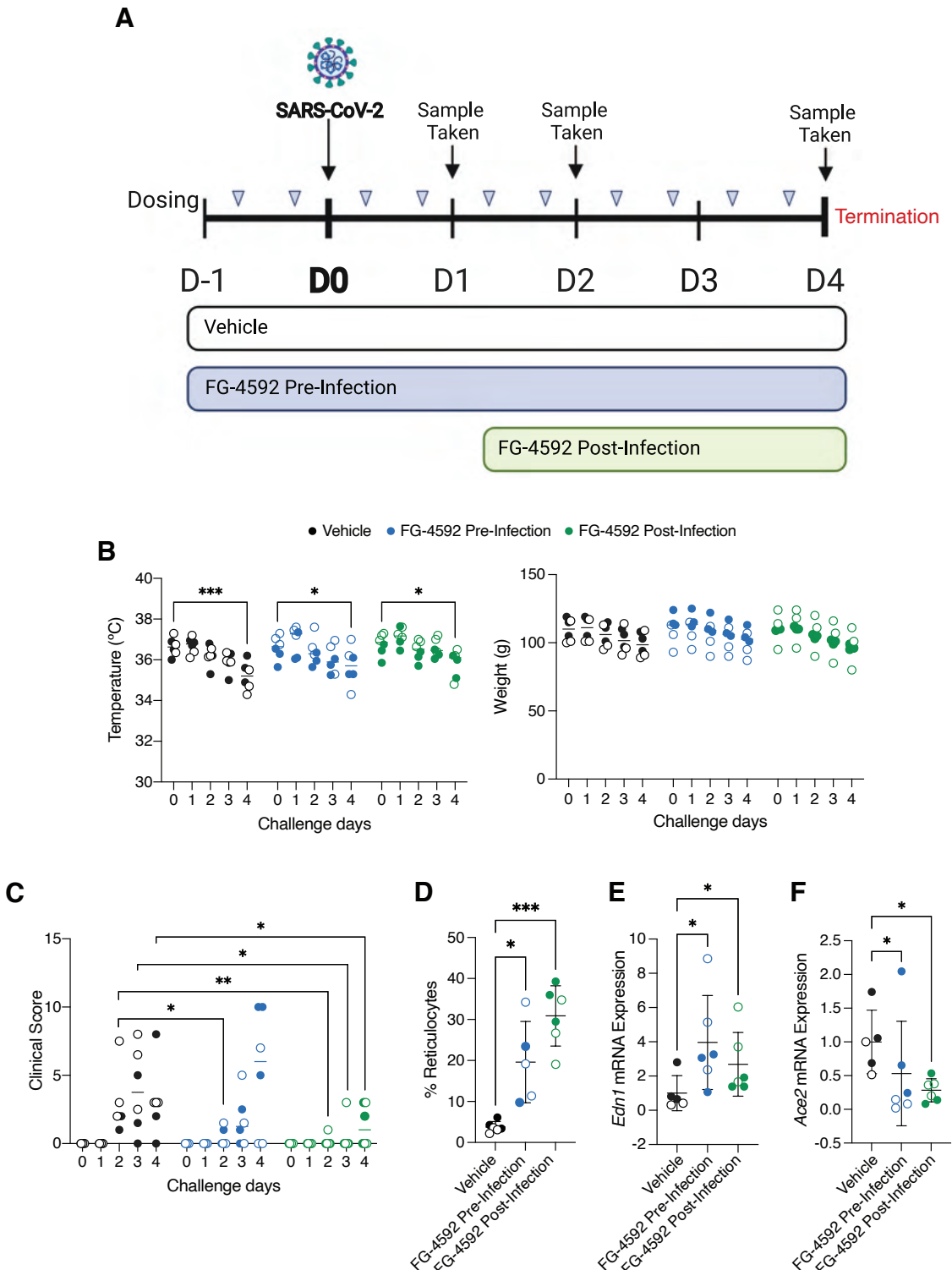


**Figure 2**

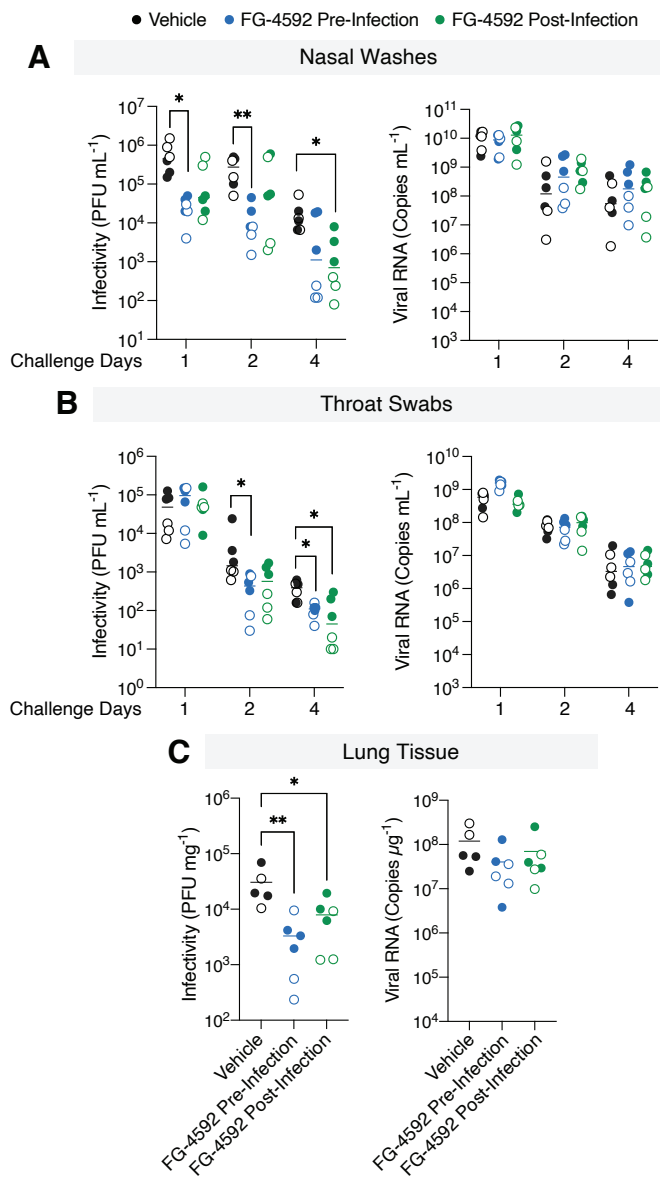


**Figure 3**

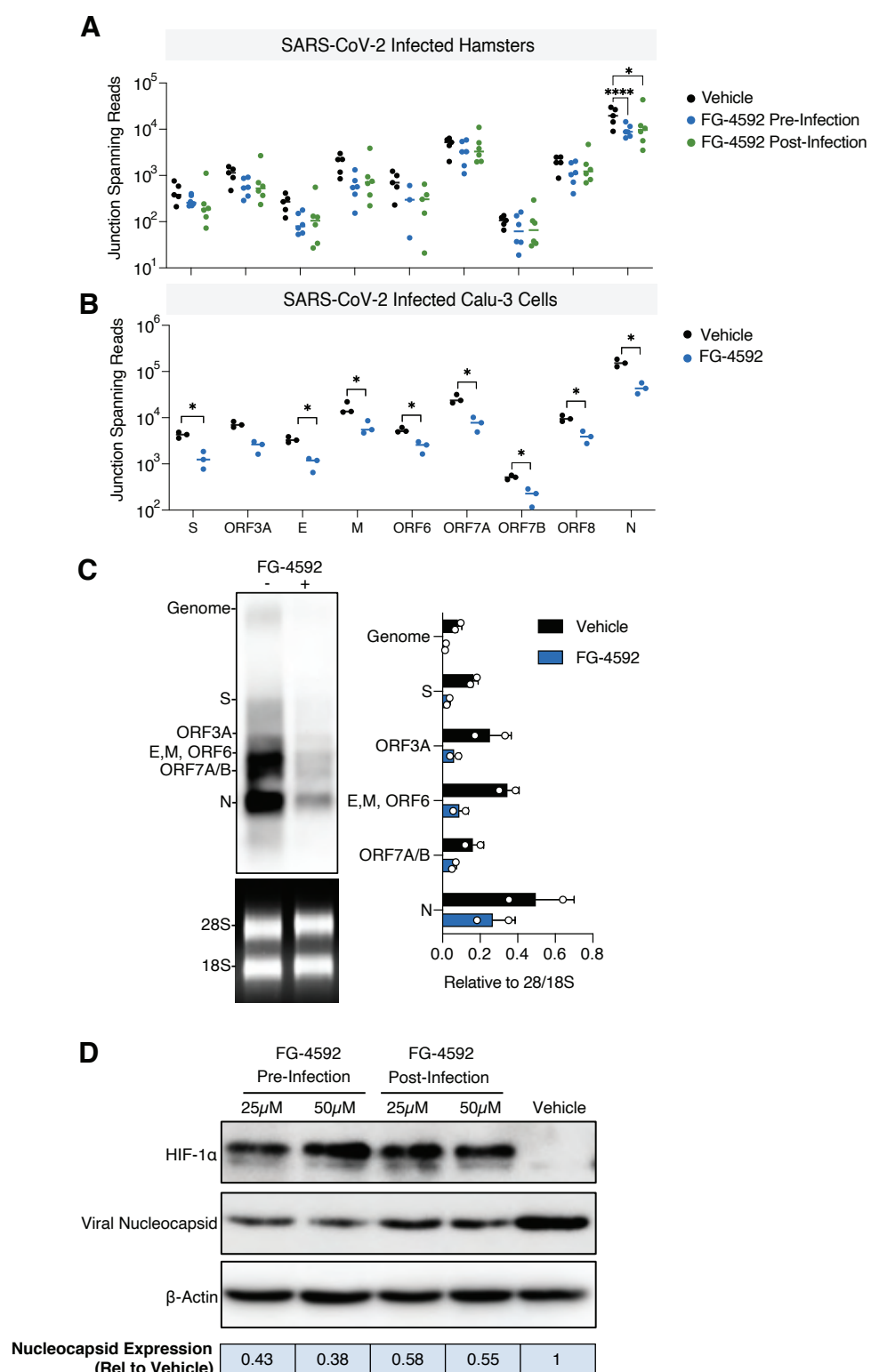


**Figure 4**

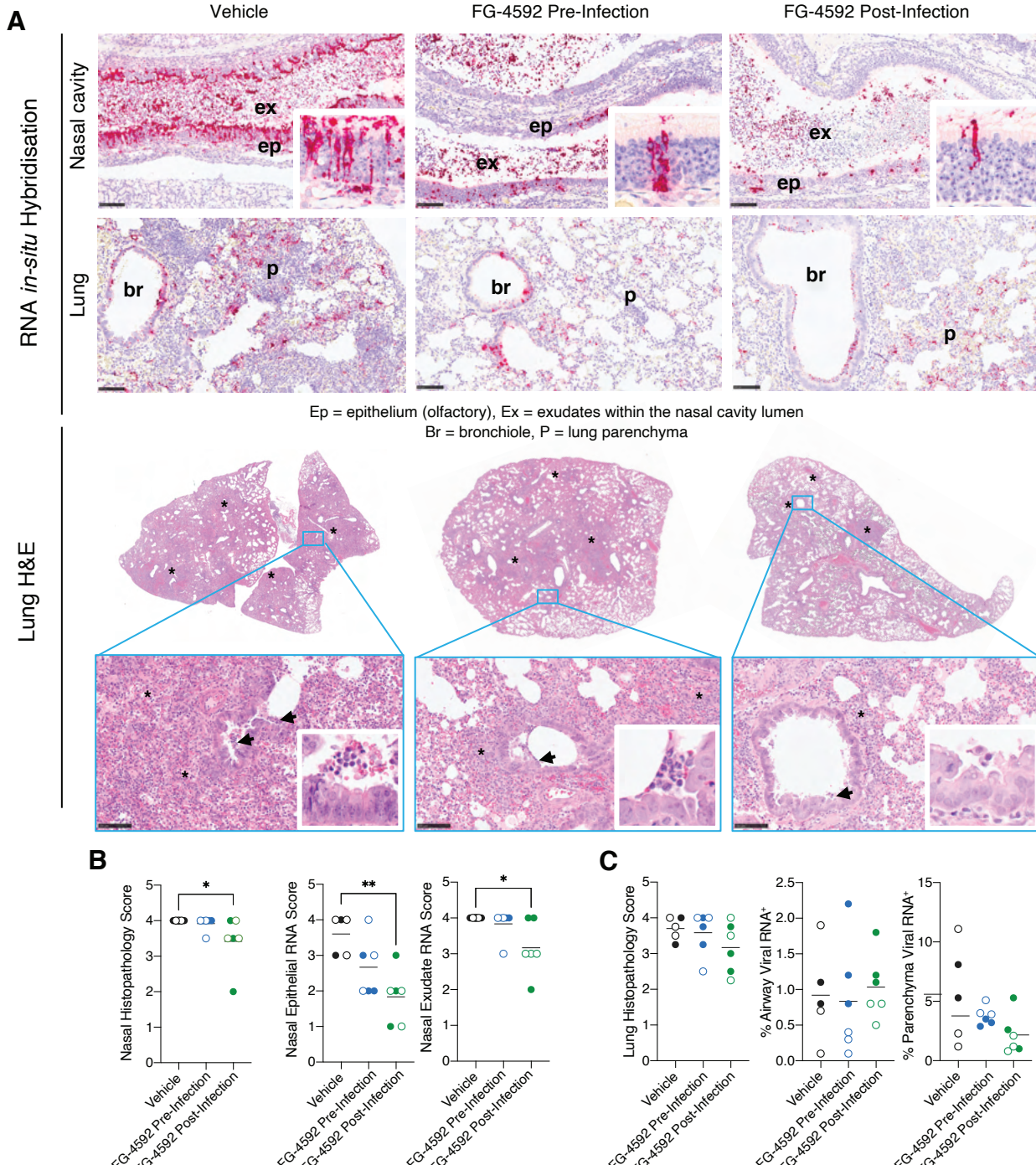


**Figure 5**

